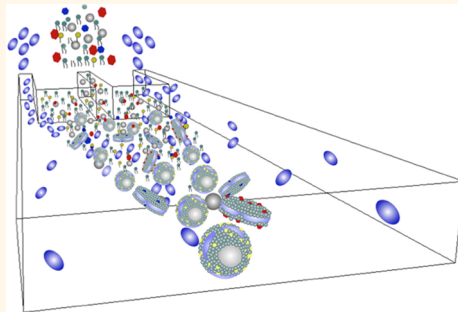


# Single Step Reconstitution of Multifunctional High-Density Lipoprotein-Derived Nanomaterials Using Microfluidics

YongTae Kim,<sup>†,‡,§,¶</sup> Francois Fay,<sup>‡,§</sup> David P. Cormode,<sup>‡,¶</sup> Brenda L. Sanchez-Gaytan,<sup>‡</sup> Jun Tang,<sup>‡</sup> Elizabeth J. Hennessy,<sup>†</sup> Mingming Ma,<sup>†</sup> Kathryn Moore,<sup>†</sup> Omid C. Farokhzad,<sup>§</sup> Edward Allen Fisher,<sup>†</sup> Willem J. M. Mulder,<sup>‡,||</sup> Robert Langer,<sup>†,\*</sup> and Zahi A. Fayad<sup>‡,\*</sup>

<sup>†</sup>David H. Koch Institute for Integrative Cancer Research, Massachusetts Institute of Technology, Cambridge, Massachusetts 02139, United States, <sup>‡</sup>Translational and Molecular Imaging Institute, Icahn School of Medicine at Mount Sinai, New York, New York 10029, United States, <sup>§</sup>Department of Anesthesiology, Brigham and Women's Hospital, Harvard Medical School, Boston, Massachusetts 02115, United States, <sup>¶</sup>Departments of Medicine (Cardiology) and Cell Biology, NYU School of Medicine, New York, New York 10016, United States, and <sup>||</sup>Department of Vascular Medicine, Academic Medical Center, Amsterdam 1105 AZ, The Netherlands. <sup>¶</sup>These authors contributed equally. <sup>†</sup>Present address: The George W. Woodruff School of Mechanical Engineering, Institute for Electronics and Nanotechnology, Parker H. Petit Institute for Bioengineering and Bioscience, Georgia Institute of Technology. <sup>¶</sup>Present address: Radiology Department, University of Pennsylvania.

**ABSTRACT** High-density lipoprotein (HDL) is a natural nanoparticle that transports peripheral cholesterol to the liver. Reconstituted high-density lipoprotein (rHDL) exhibits antiatherothrombotic properties and is being considered as a natural treatment for cardiovascular diseases. Furthermore, HDL nanoparticle platforms have been created for targeted delivery of therapeutic and diagnostic agents. The current methods for HDL reconstitution involve lengthy procedures that are challenging to scale up. A central need in the synthesis of rHDL, and multifunctional nanomaterials in general, is to establish large-scale production of reproducible and homogeneous batches in a simple and efficient fashion. Here, we present a large-scale microfluidics-based manufacturing method for single-step synthesis of HDL-mimicking nanomaterials ( $\mu$ HDL).  $\mu$ HDL is shown to have the same properties (e.g., size, morphology, bioactivity) as conventionally reconstituted HDL and native HDL. In addition, we were able to incorporate simvastatin (a hydrophobic drug) into  $\mu$ HDL, as well as gold, iron oxide, quantum dot nanocrystals or fluorophores to enable its detection by computed tomography (CT), magnetic resonance imaging (MRI), or fluorescence microscopy, respectively. Our approach may contribute to effective development and optimization of lipoprotein-based nanomaterials for medical imaging and drug delivery.



**KEYWORDS:** HDL · multifunctional · nanoparticle · reconstitution · microfluidics · high-throughput

Lipoproteins are natural nanoparticles that transport cholesterol and triglycerides throughout the body and have important roles in a variety of pathological processes,<sup>1</sup> most prominently atherosclerosis. Atherosclerosis is a progressive disease in which the buildup of cholesterol and inflammatory cells in vessel wall of arteries can eventually lead to myocardial infarction or stroke.<sup>2</sup> High levels of serum low-density lipoprotein (LDL) increase the progression of atherosclerosis and the risk of coronary artery disease.<sup>3</sup> On the other hand, high-density lipoprotein (HDL) is believed to exhibit athero-protective properties. *In vitro*, in a number of preclinical studies and in

limited clinical studies,<sup>4</sup> the mechanistic basis for a high level of HDL and a decreased risk of coronary artery disease is suggested.<sup>5</sup> These athero-protective properties include HDL's ability to remove and transport cholesterol from atherosclerotic plaques to the liver *via* a process known as reverse cholesterol transport.<sup>6,7</sup> Traditional antiatherosclerotic therapies such as statins lower LDL levels systemically, but elevating HDL levels is believed to hold great promise as an alternative strategy.<sup>8,9</sup> Among different approaches, including the application of cholesteryl ester transfer protein inhibitors,<sup>10–12</sup> direct infusion of rHDL is an emerging treatment for cardiovascular disease.

\* Address correspondence to rlanger@mit.edu, zahi.fayad@mssm.edu.

Received for review July 27, 2013 and accepted September 30, 2013.

Published online September 30, 2013  
10.1021/nn4039063

© 2013 American Chemical Society

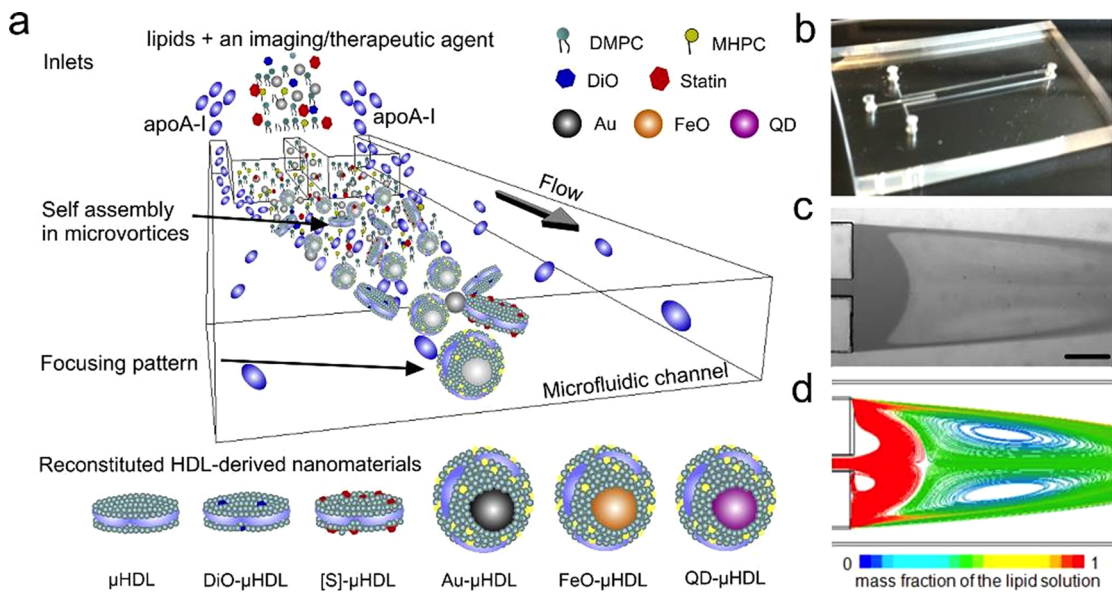


**Figure 1. Microfluidic reconstitution of HDL-derived nanomaterials ( $\mu$ HDL).** (a) A schematic depiction of a microfluidic platform that allows single-step and large-scale production of the HDL: reconstituted HDL by microfluidics ( $\mu$ HDL); DiO- $\mu$ HDL for fluorescence; [S]- $\mu$ HDL for a therapeutic platform; Au- $\mu$ HDL for CT imaging; FeO- $\mu$ HDL for MRI; and QD- $\mu$ HDL for fluorescence. (b) Photograph of the microfluidic device. (c) Microscope image of dual microvortices at  $Re = 150$ . Scale bar is  $500 \mu\text{m}$ . (d) Computational fluid dynamics simulation showing the microvortices at  $Re = 150$ .

For example, HDL infusions have been reported to modulate fatty acid metabolism<sup>13</sup> and support cholesterol efflux,<sup>14</sup> which therefore reduces myocardial lesions in a rat model<sup>15</sup> and the size of human atherosclerotic plaques or their inflammatory state.<sup>16</sup>

Moreover, HDL's endogenous character makes it well suited as a vehicle for targeted delivery of diagnostic and therapeutic agents.<sup>17–24</sup> For example, HDL nanoparticles have been reconstituted to carry inorganic nanocrystals as contrast agents for medical imaging<sup>25–28</sup> as well as to serve as delivery vehicles for siRNAs or therapeutic molecules.<sup>29,30</sup> The reconstitution of such HDL nanoparticles involves multistep processes, which are highly dependent on synthetic conditions, difficult to scale up, and laborious. For example, the cholate, sonication, and vesicle insertion methods are time-consuming, requiring at least 24 h to perform.<sup>31</sup> A central challenge in the synthesis of therapeutic and diagnostic HDL-based nanomaterials is to establish large-scale and continuous production methods with high reproducibility, yield, and homogeneity, while simultaneously decreasing the number of formulation steps.

Microfluidic technologies using diffusion, emulsification, or mixing have recently emerged for continuous formation of a variety of nanoparticles including liposomes,<sup>32,33</sup> polymeric nanoparticles,<sup>34,35</sup> and lipid-polymer hybrid nanoparticles.<sup>36,37</sup> Thanks to their ability to tune nano- and microscale interactions between precursors, microfluidic formulation processes offer effective control of the formation and characteristics of produced nanomaterials leading to a narrow size distribution and high batch-to-batch reproducibility.

In the current study, we apply the above microfluidic methodology for the synthesis of biologically active HDL-mimicking nanomaterials ( $\mu$ HDL) that can be loaded with hydrophobic molecules. The microfluidic approach enables us to tailor  $\mu$ HDL lipid composition and encapsulate compound such as simvastatin ([S]), fluorophores, or inorganic nanocrystal cores such as gold (Au), iron oxides (FeO) and quantum dots (QD) using a single-step production process that may easily be adapted for large-scale production.

In this work, we show that the physicochemical properties of  $\mu$ HDL can be readily varied and optimized by manipulating mixing speeds and the lipid to protein ratios. We demonstrate that  $\mu$ HDL has similar morphological and compositional properties to native HDL and conventionally reconstituted HDL<sup>27</sup> (rHDL). We also validate the biological properties of  $\mu$ HDL by studying its interaction with macrophages and comparing its cholesterol efflux capacity with native HDL. Finally, we demonstrate the diagnostic properties of nanocrystal loaded  $\mu$ HDL.

## RESULTS AND DISCUSSION

**Microfluidic Platform for Single Step Assembly of HDL-Derived Nanomaterials.** Multifunctional HDL-mimicking nanomaterials ( $\mu$ HDL, DiO- $\mu$ HDL, [S]- $\mu$ HDL, Au- $\mu$ HDL, FeO- $\mu$ HDL, and QD- $\mu$ HDL) were reconstituted using a single-step, self-assembly method in a single layer, 3-inlet microfluidic device (Figure 1a and Table 1). This large-scale microfluidic device (2 mm wide and  $400 \mu\text{m}$  high) generates tunable dual microvortices and a focusing pattern at Reynolds number ( $Re$ )  $\sim 150$  (Figure 1b–d), thereby allowing rapid and effective mixing of the

**TABLE 1. Experimental Setup in Microfluidics for  $\mu$ HDL Syntheses**

| inlet  | precursor  | solvent                       | (mL/min) | flow rate | Re    |
|--------|--|-------------------------------|----------|-----------|-------|
| Left   | apoA-I (0.2 mg/mL)                                 | PBS                           | 5        |           | 152.8 |
| Center | DMPC, MHPC, and imaging agents/drugs (see Table 2) | ethanol, methanol, chloroform | 1        |           |       |
| Right  | apoA-I (0.2 mg/mL)                                 | PBS                           | 5        |           |       |

**TABLE 2. Lipid, Payload, And Solvent Compositions for the Solution in the Center Inlet to the Microfluidic Channel<sup>a</sup>**

| HDL type       | lipid/imaging agent |        |                    | solvent (mL) |          |            |
|----------------|---------------------|--------|--------------------|--------------|----------|------------|
|                | DMPC                | MHPC   | imaging agent/drug | ethanol      | methanol | chloroform |
| $\mu$ HDL      | 10 mg               |        |                    | 2            |          |            |
| DiO- $\mu$ HDL | 10 mg               |        | DiO: 0.3 mg        | 2            |          |            |
| [S]- $\mu$ HDL | 20 mg               |        | Simvastatin: 4 mg  | 2            |          |            |
| Au- $\mu$ HDL  | 3.5 mg              | 1.5 mg | Au: 10 mg          | 1.75         | 0.05     | 0.2        |
| FeO- $\mu$ HDL |                     | 80 mg  | FeO: 5 mg          |              | 0.2      | 1.8        |
| QD- $\mu$ HDL  | 50 mg               |        | QD: 3 nmol         | 0.2          |          | 1.8        |

<sup>a</sup> DiO is 3,3'-dioctadecyloxacarbocyanine perchlorate. [S] is simvastatin.

**TABLE 3. Yield of the Final Product in Conventional Process (rHDL) and Microfluidics Approach ( $\mu$ HDL)**

| precursor    | yield                        |                                |
|--------------|------------------------------|--------------------------------|
|              | conventional process (n = 3) | microfluidics approach (n = 4) |
| apoA-I       | 59% $\pm$ 6                  | 57% $\pm$ 11                   |
| phospholipid | 63% $\pm$ 9                  | 53% $\pm$ 3.7                  |

solutions in the central inlet and the two outer inlets. We adjusted the type or composition of the phospholipids [e.g., 1,2-dimyristoyl-sn-glycero-3-phosphocholine (DMPC) and 1-myristoyl-2-hydroxy-sn-glycero-3-phosphocholine (MHPC)] and its mixing conditions with apolipoprotein A-I (apoA-I) by tuning the flow patterns in the microfluidic device. The solvent of the central inlet was determined by the solubility of the individual imaging agent payloads (Table 2). In this microfluidic approach, the self-assembly process occurs due to: (1) the transition of the lipid/payload from an organic solution to an aqueous one, which initiates the formation of lipid aggregates, while (2) the microvortices cause apoA-I to swiftly incorporate in the nascent aggregates, resulting in instantaneous formation of small  $\mu$ HDL nanoparticles. The conventional multistep synthesis of a 120 mg (total weight) batch of rHDL would normally first require lipid film formation (2 h), followed by lipid film hydration (3 h), 1 h of sonication and finally 16 h incubation with apoA-I.<sup>38</sup> Remarkably, in this microfluidic approach, HDL was formed instantaneously, as determined by DLS and TEM measurements (*vide infra*). This raises the prospect of on

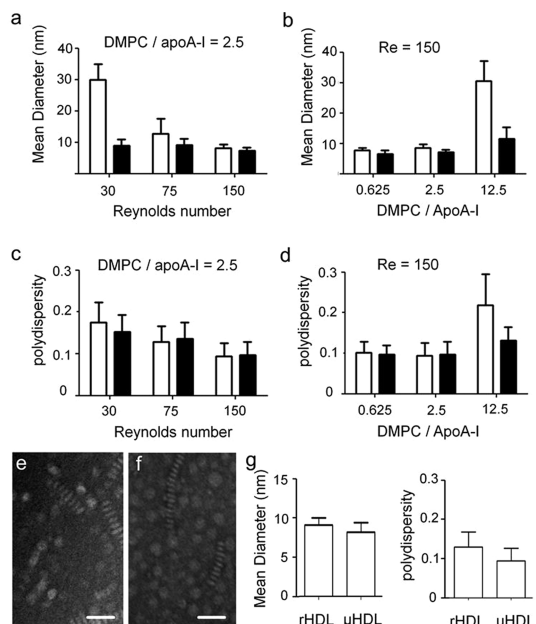


**Figure 2.**  $\mu$ HDL is controlled by Reynolds number as well as lipid-apoA-I compositions. (a) Size of  $\mu$ HDL with respect to Reynolds number, i.e., mixing speed (DMPC:apoA-I = 2.5). White column bars before purification; black bars after purification. (b) Size of  $\mu$ HDL with respect to lipid-apoA-I ratio ( $Re = 150$ ). White column bars before purification; black bars after purification. (c) Polydispersity of  $\mu$ HDL with respect to Reynolds number. (DMPC:apoA-I = 2.5). White column bars before purification; black bars after purification. (d) Polydispersity of  $\mu$ HDL with respect to lipid:apoA-I ratio ( $Re = 150$ ). White column bars before purification; black bars after purification. (e) TEM image of rHDL synthesized by sonication. Scale bar is 20 nm. (f) TEM image of  $\mu$ HDL produced using our microfluidic approach. Scale bar is 20 nm. (g) Size and polydispersity of rHDL and  $\mu$ HDL. Error bars are standard deviation.  $N = 3$ .

site or at point-of-care synthesis of these nanomedicines. Furthermore, this new microfluidic approach can result in the continuous production of  $\mu$ HDL at a rate of 420 mg/h (total weight), with minimal variability in the product while maintaining the same yield to that of conventional synthesis ( $\sim$ 57% of apoA-I) (Table 3). The microfluidic approach also has the ability for further scale up by running multiple chips in parallel. While conventional methods can also be scaled up, they would suffer from greater challenges in ensuring the desired nanoparticle properties are maintained (Tables 1–3).

**Physicochemical Properties of  $\mu$ HDL.** We investigated the size of  $\mu$ HDL as a function of the flow pattern in the microfluidic device. By varying the flow rate of each inlet (i.e., Reynolds number), we were able to judiciously adjust the  $\mu$ HDL diameter at a given lipid-to-protein ratio (i.e., DMPC:apoA-I = 2.5) (Figure 2a). By increasing the Reynolds number ( $Re$ ) from approximately 30 to 150, we were able to decrease the average size of  $\mu$ HDL from 30.0 to 8.1 nm. We noted that the solutions of DMPC and apoA-I were not well mixed at  $Re \sim 30$ , whereas they were strongly mixed at  $Re \sim 150$ . In Figure 2a the size of  $\mu$ HDL before and after

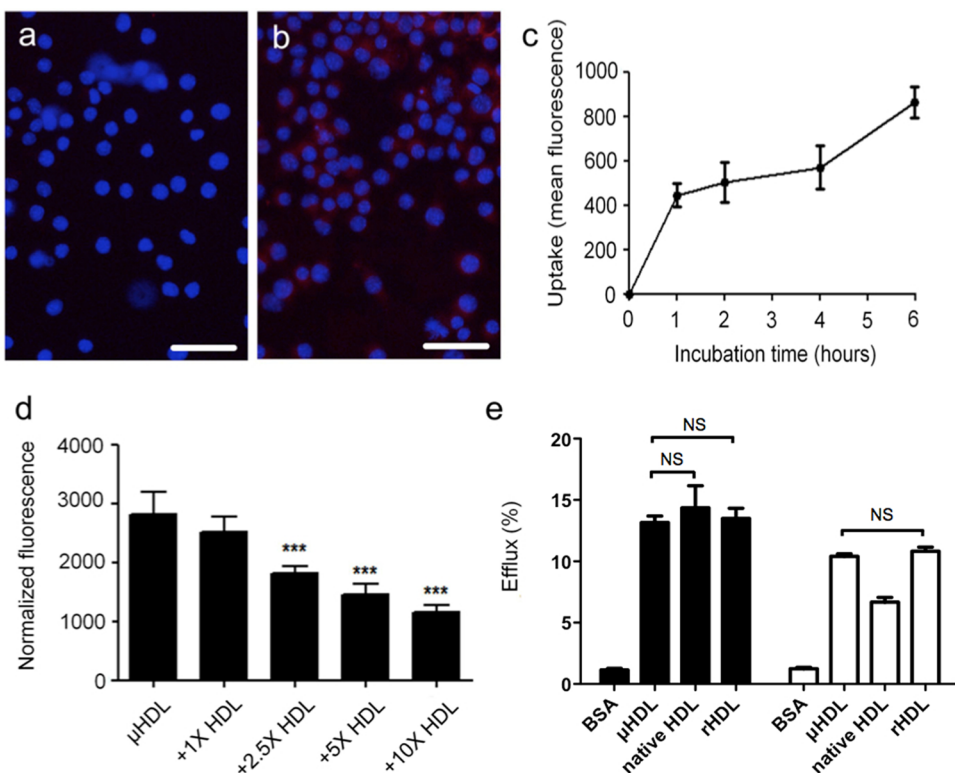


**Figure 3.**  $\mu$ HDL is bioactive. (a) Microscope image of DAPI-stained macrophages. Scale bar is 50  $\mu$ m. (b) Microscope image of DAPI-stained macrophages incubated with rhodamine-conjugated  $\mu$ HDL (shown in red). Scale bar is 50  $\mu$ m. (c)  $\mu$ HDL uptake by macrophages over time. Error bars are standard deviation.  $N = 4$ . (d) Competition assay that shows  $\mu$ HDL uptake by macrophages with respect to increasing concentrations of native HDL extracted from human plasma. Error bar is standard deviation.  $N = 5$  (\*\* $P < 0.0001$ ). (e) Cholesterol efflux of BSA,  $\mu$ HDL, native HDL, and rHDL (Black column bars BMDM; white bars J774A.1). Error bar are standard deviation.  $N = 4$ . No statistical significances were shown between HDL cases except for between  $\mu$ HDL and native HDL in J774A.1 ( $P < 0.0001$ ), while the comparisons between BSA and other HDLs showed statistical significance ( $P < 0.0001$ ).

purification indicates that for most synthesis conditions, *i.e.*, changes in  $Re$ , the size remained the same. This is indicative of a high yield of homogenously sized  $\mu$ HDL nanoparticles. We then tested how the average size changes as a function of the DMPC:apoA-I ratio at  $Re \sim 150$ . Results obtained showed that the average size of  $\mu$ HDL remained 7.6–8.5 nm as the DMPC:apoA-I ratio increased from 0.625 to 2.5 but increased to approximately 30.6 nm with a 12.5 ratio (Figure 2b). This increase is likely the result of the formation of larger lipid aggregates that do not incorporate sufficient apoA-I. Additionally, as the Reynolds number increased, the polydispersity of  $\mu$ HDL gradually decreased to approximately 0.1 (Figure 2c). We note that an excessive increase of the DMPC:apoA-I ratio led to an increase of the polydispersity to 0.218 (Figure 2d).

We then compared the structure of rHDL reconstituted using conventional multistep methods<sup>27</sup> (Figure 2e) with that of  $\mu$ HDL (Figure 2f) using transmission electron microscopy (TEM). The images revealed that both formulations adopted discoidal shape and characteristic rouleaux structures (stacks of discs on their edge), characteristic of native non-spherical HDL particles. Furthermore, dynamic light scattering confirmed that both methods resulted in

HDL nanoparticles with a similar size around 8–9 nm (Figure 2g).

**Biological Properties of  $\mu$ HDL.** HDL has been shown to bind to macrophage cells *via* several cell surface proteins such as SR-B1, ABCA1, and ABCG1.<sup>39,40</sup> We have previously shown HDL to be taken up by macrophages *via* such cell surface proteins.<sup>27,41</sup> We incubated murine macrophages with rhodamine labeled  $\mu$ HDL to probe the nanoparticle uptake and observed that the  $\mu$ HDL was taken up by macrophages in a time-dependent fashion (Figure 3a–c). Next, we performed a competitive-inhibition experiment, where  $\mu$ HDL was co-incubated with different concentrations of native HDL purified from serum. We observed a significant decrease of  $\mu$ HDL uptake in the cells with increasing concentrations of native HDL (Figure 3d), indicating that the  $\mu$ HDL was taken up by macrophages through the same pathway as native HDL. Last, we compared the macrophage cholesterol efflux capacity of  $\mu$ HDL with that of native HDL and rHDL. We found that the three HDL types ( $\mu$ -HDL, native HDL, and rHDL) produced significant and comparable efflux in both bone marrow derived macrophages (BMDM) and J774A.1 (Figure 3e). These assays demonstrated that, similar to the rHDL we previously reconstituted using

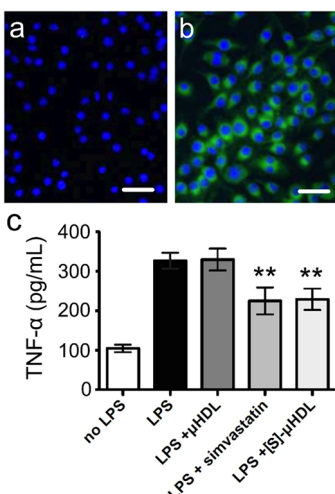


**Figure 4.**  $\mu$ HDL as hydrophobic molecules delivery agent. (a) Microscope images of DAPI-stained macrophages. Scale bar is 50  $\mu$ m. (b) Microscope images of DAPI-stained macrophages incubated with DiO- $\mu$ HDL (shown in green). Scale bar is 50  $\mu$ m. (c) TNF- $\alpha$  secretion for 24 h from preactivated macrophages incubated with [S]- $\mu$ HDL solution. TNF- $\alpha$  secretion was measured using ELISA. Error bars are standard deviation.  $N = 4$  (\*\* $P < 0.01$ ).

conventional multistep methods,<sup>27</sup>  $\mu$ HDL has similar bioactivity to native HDL.

**Incorporation of Hydrophobic Molecules into  $\mu$ HDL.** Using the single-step microfluidic approach, we were able to incorporate a fluorescent hydrophobic agent 3,3'-dioctadecyloxacarbocyanine perchlorate (DiO) or an anti-inflammatory hydrophobic drug simvastatin [S] into  $\mu$ HDL (Table 2). Nanoparticle loading of simvastatin is of interest as, when delivered orally, it is mainly confined to the liver, whereas nanoparticle formulation may allow it to be delivered to other tissues. The mean sizes of DiO- $\mu$ HDL and [S]- $\mu$ HDL, respectively, were  $7.3 \pm 1.1$  and  $32 \pm 1.3$  nm with a polydispersity of less than 0.1. The entrapment efficiencies were  $94.2 \pm 9.6\%$  for DiO (DiO (mg)/apoA-I (mg) = 0.07) and  $70.1 \pm 7.0\%$  for simvastatin (simvastatin (mg)/apoA-I (mg) = 1.4). We studied the uptake of DiO- $\mu$ HDL in murine macrophages using confocal microscopy (Figure 4a,b; see also Figure S1). Incubation of [S]- $\mu$ HDL with lipopolysaccharide (LPS) activated macrophages resulted in a 30% decrease in the secretion of tumor necrosis factor-alpha (TNF- $\alpha$ ), a pro-inflammatory cytokine (Figure 4c). Co-incubation of [S]- $\mu$ HDL with 100  $\mu$ M of mevalonate resulted in no decrease of TNF- $\alpha$  secretion, demonstrating that the effects of [S]- $\mu$ HDL are due to inhibition of the HMG-CoA reductase enzyme, as mevalonate is the product of that enzyme (Figure S2).<sup>42</sup>

**Gold Nanocrystal Core  $\mu$ HDL (Au- $\mu$ HDL).** We next incorporated gold nanocrystals into the core of  $\mu$ HDL (Table 2). The central stream contained gold nanoparticles mixed with phospholipids dissolved in a solution of ethanol, chloroform, and methanol at a ratio of

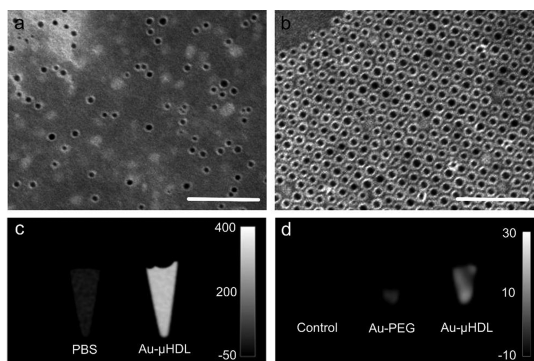


**Figure 5.** Au- $\mu$ HDL. (a and b) TEM images of Au- $\mu$ HDL (a) before and (b) after purification. Scale bar is 100 nm. (c) Phantom images of PBS and Au- $\mu$ HDL solutions using CT imaging. (d) CT images of macrophage cell pellets: non-treated cells, cells incubated with Au-PEG, and cells incubated with Au- $\mu$ HDL (Figure S4).

35:4:1, while apoA-I in a PBS buffer was infused in the outer channels at a final ratio of lipid:apoA-I ratio of 2.5:1. The crude product contained both Au- $\mu$ HDL and 'empty'  $\mu$ HDL (Figure 5a and Figure 3). Subsequently, Au- $\mu$ HDL was isolated and purified (Figure 5b) using a gradient density purification method derived from Havel's ultracentrifugation lipoprotein separation protocol.<sup>25,43</sup> Next, we tested the computed tomography (CT) detectability of Au- $\mu$ HDL phantoms (Figure 5c). We then compared the uptake of Au- $\mu$ HDL or Au-PEG (gold nanocrystals shielded by a nonspecific phospholipid-polyethylene glycol) by macrophages *in vitro* by imaging the resultant cell pellets with CT. The contrast in CT images revealed that Au- $\mu$ HDL was taken up more avidly by the cells as compared to Au-PEG (Figure 5d). Using this microfluidic method we were able to decrease the weight ratio of phospholipid:gold needed in the formation process from 5:1 for the previously reported method<sup>25</sup> to 1:1 in the microfluidic method, leading to a better yield and purer product. Furthermore, we were able to form Au- $\mu$ HDL from a range of phospholipids and their mixtures with the possibility to decrease the ratio of, or even exclude, lysolipids in the formulation (Figure S3b), which are prone to destabilize cell membranes at higher concentrations. Our single step microfluidic method not only enabled scale-up production of Au- $\mu$ HDL but also eliminated the need for long incubation steps, heating and extensive purification that were necessary in our previous methods.<sup>25</sup>

**FeO and QD Core  $\mu$ HDL (FeO- $\mu$ HDL and QD- $\mu$ HDL).** FeO nanoparticles and quantum dots were first co-disolved with the phospholipids in a solution of chloroform and methanol before being infused into the microfluidic device. We were able to produce a homogeneous population of single nanocrystal core  $\mu$ HDL after evaporating the chloroform in the produced nanoparticle solution and purifying the solution by gradient density separation (Figure 6a,b). We observed

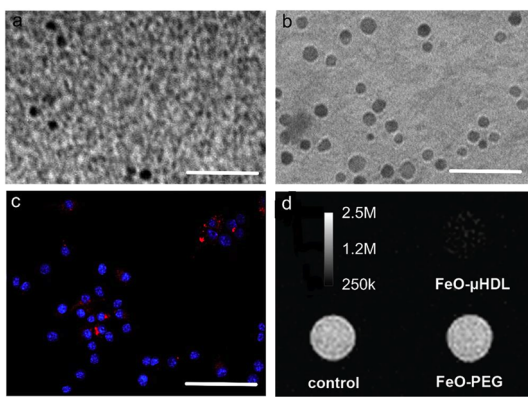


**Figure 6. QD- $\mu$ HDL and FeO- $\mu$ HDL.** (a and b) TEM images of (a) QD- $\mu$ HDL and (b) FeO- $\mu$ HDL. Scale bar is 100 nm. (c) Confocal microscopy image of macrophages incubated with QD- $\mu$ HDL. Scale bar is 100  $\mu$ m. (d)  $T_2$ -weighted magnetic resonance images of macrophage cell pellets: control (nontreated cells), cells incubated with FeO-PEG, and cells incubated with FeO- $\mu$ HDL (Figure S4).

that the nanoparticle size was dependent on the size of the quantum dots or iron oxide nanocrystals injected into the microfluidic device. Confocal images of macrophages incubated with QD- $\mu$ HDL (Figure 6c; see also Figure S5) revealed its cellular uptake. In addition, magnetic resonance images of macrophages incubated with FeO-PEG and FeO- $\mu$ HDL (Fe: 40  $\mu$ g/mL) revealed a decrease in signal intensity originating from the cell pellets incubated with FeO- $\mu$ HDL when compared to nontreated cells or cells incubated with FeO-PEG. This signal decay indicated

preferential internalization of FeO- $\mu$ HDL by macrophages.

## CONCLUSIONS

The present studies demonstrated that multifunctional HDL-mimicking nanomaterials ( $\mu$ HDL) can be reconstituted by a microfluidic production process using rapid mixing of precursors in microvortices. We identified an optimal ratio of lipid:apoA-I in the microfluidic platform and validated that  $\mu$ HDL has similar bioactivity properties to native HDL and rHDL synthesized using a conventional multistep bulk method. Using this microfluidic approach, we were able to incorporate various hydrophobic molecules and inorganic nanocrystals into  $\mu$ HDL and image these nanomaterials using computed tomography (CT), magnetic resonance imaging (MRI) and fluorescent techniques. Our new microfluidic based formulation process enables the continuous and reproducible manufacture of homogeneous HDL with the ability to readily control the properties by varying concentrations of different combinations of the precursors in a single-step procedure. This new approach could greatly contribute to effective development and optimization of HDL-based multifunctional nanomaterials for medical imaging and drug delivery. Furthermore, this microfluidic technology, once operated in parallel, has potential to facilitate reproducible and controlled synthesis of HDL nanoparticles at scales suitable for rapid clinical development and commercialization.

## METHODS

**Materials.** Myristoyl hydroxy phosphatidylcholine (MHPC), 1,2-dimyristoyl-sn-glycero-3-phosphocholine (DMPC), 1,2-distearoyl-sn-glycero-3-phosphoethanolamine-N-[methoxy(polyethylene glycol)-2000] (PEG2000-DSPE) and 1,2-dimyristoyl-sn-glycero-3-phosphoethanolamine-N-(lissamine rhodamine B sulfonyl) (Rhodamine-DMPE) were purchased from Avanti Polar Lipids, Inc. (Alabaster, AL). 3,3'-Diiodocadecyoxacarbocyanine perchlorate (DiO) was purchased from Invitrogen. Oleic acid coated iron oxide nanoparticles were purchased from NN Laboratories (Fayetteville, AR). Dodecanethiol coated gold nanoparticles were synthesized as described previously.<sup>25</sup> The 650 nm emitting CdSe/CdS/CdZnS/Zn core-shell-shell quantum dots were synthesized as described previously.<sup>28</sup> Apolipoprotein A-1 was a kind gift of CSL Ltd. (Parkville, Australia).

**Microfluidic Device Design and Fabrication.** Our microfluidic device had three inlet channels (with rectangular cross sections ( $200 \times 400 \mu\text{m}^2$ ) converged to create a single mixing zone with dimensions 2 mm wide, 400  $\mu\text{m}$  high, and 20 mm long. The device was made of polydimethylsiloxane (PDMS) (SYLGARD 184, Dow Corning, Midland, MI) using standard soft-lithography techniques.<sup>44</sup>

**Flow Visualization.** Flow patterns in the single mixing zone of the microfluidic device were visualized using a stereo microscope (Leica M125, Leica Microsystems, Bannockburn, IL). In the visualization, the central stream has a 10:1 ratio of deionized water and black ink and the outer streams have deionized water.

**Reynolds Number and Flow Rate.** Syringe pumps (NE-1010-U, Kats Scientific) were used to regulate flow rates in the microfluidic device. The flow rate in the outer streams was set to 5 mL/min (total 10 mL/min for both outer channels), while the

flow rate in the central stream was 1 mL/min. Reynolds number ( $Re$ ) was calculated using the following equation:<sup>45</sup>

$$Re = \frac{\rho U D_h}{\mu} = \frac{\rho U}{\mu} \frac{2wh}{w+h} = \frac{\rho}{\mu} \frac{2Q}{w+h}$$

where  $Q$  is the flow rate;  $\mu$  represents the fluid's viscosity;  $w$  and  $h$  represent the channel width (2000  $\mu\text{m}$ ) and height (400  $\mu\text{m}$ );  $\rho$  represents the fluid's density;  $U$  represents the fluid's average velocity.

**Numerical Simulations.** Computational fluid dynamics simulations predicted the flow field using the commercial CFD solver (SC/Tetra, CRADLE, Beavercreek, OH). We assumed a Newtonian fluid with the properties of water at room temperature and no-slip boundary conditions on all the walls. Mesh independence study was conducted. The convergence limit of the velocity was set to 0.1%, in which the mass fraction reached the asymptotic value within 0.01%.

**$\mu$ HDL Synthesis.** Organic solution containing 5 mg/mL of phospholipids (DMPC) was injected into the middle inlet channel of the microfluidics device at a rate of 1 mL/min using a programmable syringe pump, while aqueous solutions of apoA-I (0.2 mg/mL) in PBS were injected in both the outer channels at a rate of 5 mL/min.  $\mu$ HDL produced through controlled mixing of the solutions was collected at the outlet of the device.  $\mu$ HDL was then washed 3 times in PBS and concentrated to desired volumes using 10 000 MWCO centrifugal concentrators.

**Production Rate.** The production rate was calculated using the following formula:

$$\text{Production rate (total wt/h)} = [C_1 \cdot (fr_1 + fr_1) + C_2 \cdot fr_2]$$

where  $C_1$  represents the concentration of the apoA-I in the aqueous solution (mg/mL);  $C_2$  represents the concentration of the phospholipid in the organic solution (mg/mL);  $f_{r1}$  represents the flow rate of the aqueous solutions (mL/h) and  $f_{r2}$  represents the flow rate of the organic solution (mL/h). To load  $\mu$ HDL with either hydrophobic molecules or nanocrystals, we used the above method with slight alterations as indicated in Table 2.

**Gradient Density Purification.** Nanocrystal loaded HDL was separated from empty  $\mu$ HDL using a dual density based centrifugation method adapted from Havel's lipoprotein separation method.<sup>43</sup> Briefly, 200  $\mu$ L of  $\mu$ HDL mixture in PBS was carefully added on top of 1 mL of a 30% (w/w) KBr solution and subsequently centrifuged for 1 h at 14 100g. During centrifugation,  $\mu$ HDL remained within the top layer, while denser nanocrystals loaded HDL pelleted into the KBr layer. After centrifugation, the top layer was discarded, while the remaining solution was collected and its content washed three times with PBS. This above-mentioned procedure was performed twice before the particles were concentrated to the desired volume.

**Dynamic Light Scattering.** The nanoparticle samples were diluted in deionized filtrated water (18  $\Omega$  cm) and nanoparticle size was analyzed a minimum of three times for each sample by dynamic light scattering (DLS) using a ZetaPALS system (Brookhaven Instruments Corporation).

**Transmission Electron Microscopy.** HDL sample solutions were transferred to an ammonium acetate buffer solution, then negatively stained using an ammonium acetate buffer containing 2% sodium phosphotungstate.<sup>46</sup> Drops of samples were then placed onto 100 mesh Formvar coated nickel grids (Electron Microscopy Sciences) and allowed to air-dry. Grids were imaged using a Hitachi 7650 microscope operated at 80 kV and connected to a digital camera (Scientific Instruments and Applications) controlled by Maxim CCD software.

**DiO Loading Measurements.** HDL solution samples were completely dried for 16 h in a desiccator, then solubilized in ethanol. Solutions were then centrifuged and the supernatants were collected. DiO concentrations were then quantified by measuring sample absorbance at 480 nm using a Spectramax m5 plate reader (Molecular Devices, Sunnyvale, CA).

**Simvastatin Loading Measurements.** HDL solution samples were dried for 16 h in a desiccator then solubilized in acetonitrile. Acetonitrile solutions were then centrifuged and the supernatants collected. Simvastatin concentrations were then measured using reverse phase C18 column connected to a Shimadzu HPLC system.

**Cell Propagation.** Murine sarcoma macrophage cells J774A.1 (ATCC, Manassas, VA) were propagated in Dulbecco's Modified Eagle Medium supplemented with 1% streptomycin/penicillin (Cellgro Mediatech Manassas, VA) and 10% fetal bovine serum (Sigma-Aldrich, St. Louis, MO). Before experiments, cells were detached, washed in PBS, and counted. Defined numbers of cells were then seeded and left overnight to adhere. Immediately before experiments were initiated, the media was replaced with fresh media.

**Rhodamine Assay.** Rhodamine labeled  $\mu$ HDL was incubated with murine macrophages and subsequently washed with PBS to discard nonbound/internalized particles. In competition–inhibition experiments, macrophages were co-incubated with a fixed concentration of the rhodamine labeled  $\mu$ HDL (21.4  $\mu$ g/mL apoA-I) and increasing amounts of native murine HDL extracted from serum.

**Fluorescence/Confocal Microscopy.** Macrophages were seeded on microscope chamber slides and allowed to adhere overnight. The cell media was then refreshed and cells incubated for 2 h with various nanoparticle solutions. After incubation, slides were washed three times with PBS and cells were fixed with 4% paraformaldehyde (PFA) for 30 min at 37 °C. Slides were then washed again three times with PBS and mounted with mounting media containing DAPI (Vectashield, Vector Laboratories). Epifluorescence images were taken using an Olympus 1  $\times$  71 fluorescence Inverted Microscope. Confocal images were taken using a Leica TCS SP5 DM confocal using a sequential setup and excitation at 405 nm.

**Cholesterol Efflux Assay.** J774A.1 macrophages and murine bone marrow derived macrophages (BMDM) were first incubated

with media containing 0.5  $\mu$ Ci/mL [<sup>3</sup>H]-cholesterol and 0.34  $\mu$ M phorbol 12-myristate 13-acetate for 24 h. Cells were subsequently washed twice with PBS and incubated with media containing 0.34  $\mu$ M phorbol 12-myristate 13-acetate and 2 mg/mL fatty acid-free albumin. After washing, cells were incubated for 16 h with different HDL solutions (50  $\mu$ g/mL by protein content). Cell media was then removed and the cells were lysed in 0.1 N NaOH solution. [<sup>3</sup>H]-Cholesterol contents of media and cell lysates were measured by liquid scintillation counting.

**TNF- $\alpha$  Secretion Assay.** J774A.1 cells were seeded in 96-well plates (25 000 cells/well) and allowed to adhere overnight. Cells were then activated for 6 h with 300 units/mL of interferon- $\gamma$ , then 16 h with 300 units/mL of interferon- $\gamma$  and 25 ng/mL of LPS. Cells were then incubated for 24 h with serum free media containing either 10  $\mu$ M of free simvastatin, [S]- $\mu$ HDL equivalent to 10  $\mu$ M simvastatin or an equal amount of  $\mu$ HDL. The resulting TNF- $\alpha$  concentration in the media was measured using a TNF- $\alpha$  ELISA kit (Invitrogen, CA).

**Au- $\mu$ HDL Incubation with Macrophages.** Three million cells/dish were seeded in 100 nm tissue culture dishes and allowed to adhere overnight. Cells were then incubated for 8 h with 10 mL of media containing 1.25 mg (gold content) of Au nanoparticles. Cells were then washed three times with PBS, collected using cell scrapers and centrifuged for 5 min at 500g. Cells were resuspended in 4% PFA and centrifuged to form a pellet.

**FeO- $\mu$ HDL Incubation with Macrophages.** A total of 500 000 cells/well were seeded in 6-well plates and allowed to adhere overnight. The cells were then incubated with 2 mL of media containing FeO nanoparticles at a concentration of 40  $\mu$ g Fe/mL for 7 h. Cells were then washed three times with PBS, collected using scrapers and centrifuged for 5 min at 500g. Cells were resuspended in 4% PFA and allowed to form a pellet.

**CT Scanning.** Particle solutions and cell pellets were imaged on 256-slice Brilliance iCT scanner (Philips Medical Systems, Nederland B.V., The Netherlands). Gold attenuation values (expressed in Hounsfield units (HU)) were the average obtained from 3 selected regions of interest using the instrument's software and converted to Au concentration using a predetermined formula.<sup>47</sup> The CT images presented were prepared using OsiriX 32-bit (Geneva, Switzerland).

**MR Scanning.**  $T_2$ -weighted cell pellet images were obtained using a 7T MRI system (Bruker Instruments) with a gradient echo sequence: echo time, 2 ms; repetition time, 2000 ms; field of view, 20  $\times$  20  $\times$  10 mm; imaging matrix, 128  $\times$  128  $\times$  16; flip angle, 3°. The images presented in the manuscript were prepared using the Osirix software mentioned above.

**Relaxometry.** Iron oxide HDL samples were completely dried for 16 h in a desiccator then solubilized in ethanol. Samples were then incubated with 1 N HCl at 40 °C until total dissolution.  $T_1$  measurements of the nanoparticle solutions were performed on a 60 MHz Bruker Minispec (Bruker Medical BmbH, Ettingen) operating at 40 °C. Iron concentration of the samples was then calculated using the calibration curve of  $1/T_1$  measurements of samples containing a known quantity of iron oxide.

**Conflict of Interest:** The authors declare the following competing financial interest(s): In compliance with the Brigham and Women's Hospital and Harvard Medical School institutional guidelines, R.L. and O.C.F. disclose their financial interest in BIND Therapeutics, Selecta Biosciences, and Blend Therapeutics, three biotechnology companies developing nanoparticle technologies for medical applications. BIND, Selecta, and Blend did not support the aforementioned research, and currently these companies have no rights to any technology or intellectual property developed as part of this research.

**Acknowledgment.** We thank MIT Microsystems Technology Laboratory (MTL) for the use of the fabrication equipment. We would also like to thank the Microscopy Shared Resource Facility, the Flow Cytometry Shared Resource Facility and the Department of Pathology of Icahn School of Medicine at Mount Sinai for the use of their equipment. Additionally, we also thank Lazar Fleysher for his help with MR imaging. We finally thank CSL Ltd, Parkville, Australia for their kind gift of apolipoprotein A-I. This research was supported by the National Heart, Lung,

and Blood Institute (NHLBI) and the National Institutes of Health (NIH), as a Program of Excellence in Nanotechnology (PEN) Award, Contract No. HHSN268201000045C (Z.A.F. and R.L.), the National Cancer Institute Grant CA151884 (R.L. and O.C.F.), the David H. Koch—Prostate Cancer Foundation Award in Nanotherapeutics (R.L. and O.C.F.), R00 EB012165 (D.P.C.), American Heart Association Award No. 13PRE14350020-Founders (J.T.), and R01 CA155432 (W.J.M.M.).

*Supporting Information Available:* Supporting information with 5 figures includes confocal microscopy images and flow cytometry data. This material is available free of charge via the Internet at <http://pubs.acs.org>.

## REFERENCES AND NOTES

- Bricarello, D. A.; Mills, E. J.; Petrlova, J.; Voss, J. C.; Parikh, A. N. Ganglioside Embedded in Reconstituted Lipoprotein Binds Cholera Toxin with Elevated Affinity. *J. Lipid Res.* **2010**, *51*, 2731–2738.
- Libby, P.; Ridker, P. M.; Maseri, A. Inflammation and Atherosclerosis. *Circulation* **2002**, *105*, 1135–1143.
- Lusis, A. J. Atherosclerosis. *Nature* **2000**, *407*, 233–241.
- Nissen, S. E.; Tsunoda, T.; Tuzcu, E. M.; Schoenhagen, P.; Cooper, C. J.; Yasin, M.; Eaton, G. M.; Lauer, M. A.; Sheldon, W. S.; Grines, C. L.; et al. Effect of Recombinant Apo-a-I Milano on Coronary Atherosclerosis in Patients with Acute Coronary Syndromes: A Randomized Controlled Trial. *JAMA* **2003**, *290*, 2292–2300.
- Gordon, D. J.; Rifkind, B. M. High-Density Lipoprotein—the Clinical Implications of Recent Studies. *N. Engl. J. Med.* **1989**, *321*, 1311–1316.
- Linsel-Nitschke, P.; Tall, A. R. Hdl as a Target in the Treatment of Atherosclerotic Cardiovascular Disease. *Nat. Rev. Drug Discovery* **2005**, *4*, 193–205.
- Hersberger, M.; von Eckardstein, A. Modulation of High-Density Lipoprotein Cholesterol Metabolism and Reverse Cholesterol Transport. *Handb. Exp. Pharmacol.* **2005**, *537*–561.
- Watts, G. F.; Burnett, J. R. Hdl Revisited: New Opportunities for Managing Dyslipoproteinemia and Cardiovascular Disease. *Clin. Biochem. Rev.* **2004**, *25*, 7–18.
- Nicholls, S. J.; Uno, K.; Tuzcu, E. M.; Nissen, S. E. Lessons from Coronary Intravascular Ultrasound on the Importance of Raising High-Density Lipoprotein Cholesterol. *Curr. Atheroscler. Rep.* **2010**, *12*, 301–307.
- Vergeer, M.; Bots, M. L.; van Leuven, S. I.; Basart, D. C.; Sijbrands, E. J.; Evans, G. W.; Grobbee, D. E.; Visseren, F. L.; Stalenhoef, A. F.; Stroes, E. S.; et al. Cholesteroyl Ester Transfer Protein Inhibitor Torcetrapib and Off-Target Toxicity: A Pooled Analysis of the Rating Atherosclerotic Disease Change by Imaging with a New Cetp Inhibitor (Radiance) Trials. *Circulation* **2008**, *118*, 2515–2522.
- Brousseau, M. E.; Schaefer, E. J.; Wolfe, M. L.; Bloedon, L. T.; Digenio, A. G.; Clark, R. W.; Mancuso, J. P.; Rader, D. J. Effects of an Inhibitor of Cholesteroyl Ester Transfer Protein on Hdl Cholesterol. *N. Engl. J. Med.* **2004**, *350*, 1505–1515.
- Krishna, R.; Anderson, M. S.; Bergman, A. J.; Jin, B.; Fallon, M.; Cote, J.; Rosko, K.; Chavez-Eng, C.; Lutz, R.; Bloomfield, D. M.; et al. Effect of the Cholesteroyl Ester Transfer Protein Inhibitor, Anacetrapib, on Lipoproteins in Patients with Dyslipidaemia and on 24-H Ambulatory Blood Pressure in Healthy Individuals: Two Double-Blind, Randomised Placebo-Controlled Phase I Studies. *Lancet* **2007**, *370*, 1907–1914.
- Drew, B. G.; Carey, A. L.; Natoli, A. K.; Formosa, M. F.; Vizi, D.; Reddy-Luthmoodoo, M.; Weir, J. M.; Barlow, C. K.; van Hall, G.; Meikle, P. J.; et al. Reconstituted High-Density Lipoprotein Infusion Modulates Fatty Acid Metabolism in Patients with Type 2 Diabetes Mellitus. *J. Lipid Res.* **2011**, *52*, 572–581.
- Hoang, A.; Drew, B. G.; Low, H.; Remaley, A. T.; Nestel, P.; Kingwell, B. A.; Sviridov, D. Mechanism of Cholesterol Efflux in Humans after Infusion of Reconstituted High-Density Lipoprotein. *Eur. Heart J.* **2012**, *33*, 657–665.
- Borthwick, F.; Warnakula, S.; Mangat, R.; Uwiera, R. R.; Russell, J. C.; Kelly, S. E.; Lee, C. Y.; Hryshko, L.; Mamo, J. C.; Rye, K. A.; et al. Apo-a-1 Infusion Reduces Arterial Cholesterol and Myocardial Lesions in a Rat Model of Cardiac Dysfunction and Insulin Resistance. *Atherosclerosis* **2012**, *222*, 402–408.
- Shaw, J. A.; Bobik, A.; Murphy, A.; Kanellakis, P.; Blomberg, P.; Mukhamedova, N.; Woollard, K.; Lyon, S.; Sviridov, D.; Dart, A. M. Infusion of Reconstituted High-Density Lipoprotein Leads to Acute Changes in Human Atherosclerotic Plaque. *Circ. Res.* **2008**, *103*, 1084–1091.
- Glickson, J. D.; Lund-Katz, S.; Zhou, R.; Choi, H.; Chen, I. W.; Li, H.; Corbin, I.; Popov, A. V.; Cao, W.; Song, L.; et al. Lipoprotein Nanoplatform for Targeted Delivery of Diagnostic and Therapeutic Agents. *Mol. Imaging* **2008**, *7*, 101–110.
- Heeren, J.; Beisiegel, U.; Grewal, T. Apolipoprotein E Recycling: Implications for Dyslipidemia and Atherosclerosis. *Arterioscler., Thromb., Vasc. Biol.* **2006**, *26*, 442–448.
- Briley-Saebo, K. C.; Geminatti-Crich, S.; Cormode, D. P.; Barazza, A.; Mulder, W. J.; Chen, W.; Giovenzana, G. B.; Fisher, E. A.; Aime, S.; Fayad, Z. A. High-Relaxivity Gadolinium-Modified High-Density Lipoproteins as Magnetic Resonance Imaging Contrast Agents. *J. Phys. Chem. B* **2009**, *113*, 6283–6289.
- Cormode, D. P.; Frias, J. C.; Ma, Y.; Chen, W.; Skajaa, T.; Briley-Saebo, K.; Barazza, A.; Williams, K. J.; Mulder, W. J.; Fayad, Z. A.; et al. Hdl as a Contrast Agent for Medical Imaging. *Clin. Lipidol.* **2009**, *4*, 493–500.
- Mulder, W. J.; Strijkers, G. J.; van Tilborg, G. A.; Cormode, D. P.; Fayad, Z. A.; Nicolay, K. Nanoparticulate Assemblies of Amphiphiles and Diagnostically Active Materials for Multimodality Imaging. *Acc. Chem. Res.* **2009**, *42*, 904–914.
- Ahmed, W.; Orasanu, G.; Nehra, V.; Asatryan, L.; Rader, D. J.; Ziouzenkova, O.; Plutzky, J. High-Density Lipoprotein Hydrolysis by Endothelial Lipase Activates Pparalpha: A Candidate Mechanism for High-Density Lipoprotein-Mediated Depression of Leukocyte Adhesion. *Circ. Res.* **2006**, *98*, 490–498.
- Chen, W.; Jarzyna, P. A.; van Tilborg, G. A.; Nguyen, V. A.; Cormode, D. P.; Klink, A.; Griffioen, A. W.; Randolph, G. J.; Fisher, E. A.; Mulder, W. J.; et al. Rgd Peptide Functionalized and Reconstituted High-Density Lipoprotein Nanoparticles as a Versatile and Multimodal Tumor Targeting Molecular Imaging Probe. *FASEB J.* **2010**, *24*, 1689–1699.
- Luthi, A. J.; Zhang, H.; Kim, D.; Giljohann, D. A.; Mirkin, C. A.; Thaxton, C. S. Tailoring of Biomimetic High-Density Lipoprotein Nanostructures Changes Cholesterol Binding and Efflux. *ACS Nano* **2012**, *6*, 276–285.
- Cormode, D. P.; Skajaa, T.; van Schooneveld, M. M.; Koole, R.; Jarzyna, P.; Lobatto, M. E.; Calcagno, C.; Barazza, A.; Gordon, R. E.; Zanzonico, P.; et al. Nanocrystal Core High-Density Lipoproteins: A Multimodality Contrast Agent Platform. *Nano Lett.* **2008**, *8*, 3715–3723.
- Cormode, D. P.; Roessl, E.; Thran, A.; Skajaa, T.; Gordon, R. E.; Schlamka, J. P.; Fuster, V.; Fisher, E. A.; Mulder, W. J.; Proksa, R.; et al. Atherosclerotic Plaque Composition: Analysis with Multicolor Ct and Targeted Gold Nanoparticles. *Radiology* **2010**, *256*, 774–782.
- Skajaa, T.; Cormode, D. P.; Jarzyna, P. A.; Delshad, A.; Blachford, C.; Barazza, A.; Fisher, E. A.; Gordon, R. E.; Fayad, Z. A.; Mulder, W. J. The Biological Properties of Iron Oxide Core High-Density Lipoprotein in Experimental Atherosclerosis. *Biomaterials* **2011**, *32*, 206–213.
- Skajaa, T.; Zhao, Y.; van den Heuvel, D. J.; Gerritsen, H. C.; Cormode, D. P.; Koole, R.; van Schooneveld, M. M.; Post, J. A.; Fisher, E. A.; Fayad, Z. A.; et al. Quantum Dot and Cy5.5 Labeled Nanoparticles to Investigate Lipoprotein Biointeractions via Forster Resonance Energy Transfer. *Nano Lett.* **2010**, *10*, 5131–5138.
- Yang, S.; Damiano, M. G.; Zhang, H.; Tripathy, S.; Luthi, A. J.; Rink, J. S.; Ugolkov, A. V.; Singh, A. T. K.; Dave, S. S.; Gordon, L. I.; et al. Biomimetic, Synthetic Hdl Nanostructures for Lymphoma. *Proc. Natl. Acad. Sci. U.S.A.* **2013**, *110*, 2511–2516.

30. McMahon, K. M.; Mutharasan, R. K.; Tripathy, S.; Veliceasa, D.; Bobeica, M.; Shumaker, D. K.; Luthi, A. J.; Helfand, B. T.; Ardehali, H.; Mirkin, C. A.; *et al.* Biomimetic High Density Lipoprotein Nanoparticles for Nucleic Acid Delivery. *Nano Lett.* **2011**, *11*, 1208–1214.
31. Jonas, A. Synthetic Substrates of Lecithin: Cholesterol Acyltransferase. *J. Lipid Res.* **1986**, *27*, 689–698.
32. Jahn, A.; Stavis, S. M.; Hong, J. S.; Vreeland, W. N.; DeVoe, D. L.; Gaitan, M. Microfluidic Mixing and the Formation of Nanoscale Lipid Vesicles. *ACS Nano* **2010**, *4*, 2077–2087.
33. Hong, J. S.; Stavis, S. M.; DePaoli Lacerda, S. H.; Locascio, L. E.; Raghavan, S. R.; Gaitan, M. Microfluidic Directed Self-Assembly of Liposome-Hydrogel Hybrid Nanoparticles. *Langmuir* **2010**, *26*, 11581–11588.
34. Karnik, R.; Gu, F.; Basto, P.; Cannizzaro, C.; Dean, L.; Kyei-Manu, W.; Langer, R.; Farokhzad, O. C. Microfluidic Platform for Controlled Synthesis of Polymeric Nanoparticles. *Nano Lett.* **2008**, *8*, 2906–2912.
35. Kolishetti, N.; Dhar, S.; Valencia, P. M.; Lin, L. Q.; Karnik, R.; Lippard, S. J.; Langer, R.; Farokhzad, O. C. Engineering of Self-Assembled Nanoparticle Platform for Precisely Controlled Combination Drug Therapy. *Proc. Natl. Acad. Sci. U.S.A.* **2010**, *107*, 17939–17944.
36. Kim, Y.; Lee Chung, B.; Ma, M.; Mulder, W. J.; Fayad, Z. A.; Farokhzad, O. C.; Langer, R. Mass Production and Size Control of Lipid-Polymer Hybrid Nanoparticles through Controlled Microvortices. *Nano Lett.* **2012**, *12*, 3587–3591.
37. Mieszawska, A. J.; Kim, Y.; Gianella, A.; van Rooy, I.; Priem, B.; Labarre, M. P.; Ozcan, C.; Cormode, D. P.; Petrov, A.; Langer, R.; *et al.* Synthesis of Polymer-Lipid Nanoparticles for Image-Guided Delivery of Dual Modality Therapy. *Bioconjugate Chem.* **2013**, *24*, 1429–1434.
38. Jonas, A. Reconstitution of High-Density Lipoproteins. *Methods Enzymol.* **1986**, *128*, 553–582.
39. Tall, A. R. Cholesterol Efflux Pathways and Other Potential Mechanisms Involved in the Athero-Protective Effect of High Density Lipoproteins. *J. Intern. Med.* **2008**, *263*, 256–273.
40. Acton, S.; Rigotti, A.; Landschulz, K. T.; Xu, S.; Hobbs, H. H.; Krieger, M. Identification of Scavenger Receptor Sr-Bi as a High Density Lipoprotein Receptor. *Science* **1996**, *271*, 518–520.
41. Cormode, D. P.; Chandrasekar, R.; Delshad, A.; Briley-Saebo, K. C.; Calcagno, C.; Barazzza, A.; Mulder, W. J.; Fisher, E. A.; Fayad, Z. A. Comparison of Synthetic High Density Lipoprotein (HDL) Contrast Agents for Mr Imaging of Atherosclerosis. *Bioconjugate Chem.* **2009**, *20*, 937–943.
42. Marz, W.; Koenig, W. HMG-CoA Reductase Inhibition: Anti-Inflammatory Effects Beyond Lipid Lowering? *J. Cardiovasc. Risk* **2003**, *10*, 169–179.
43. Havel, R. J.; Eder, H. A.; Bragdon, J. H. The Distribution and Chemical Composition of Ultracentrifugally Separated Lipoproteins in Human Serum. *J. Clin. Invest.* **1955**, *34*, 1345–1353.
44. Qin, D.; Xia, Y.; Whitesides, G. M. Soft Lithography for Micro- and Nanoscale Patterning. *Nat. Protoc.* **2010**, *5*, 491–502.
45. Squires, T. M.; Quake, S. R. Microfluidics: Fluid Physics at the Nanoliter Scale. *Rev. Mod. Phys.* **2005**, *77*, 977–1026.
46. Forte, T. M.; Nordhausen, R. W. Electron Microscopy of Negatively Stained Lipoproteins. *Methods Enzymol.* **1986**, *128*, 442–457.
47. Mieszawska, A. J.; Gianella, A.; Cormode, D. P.; Zhao, Y.; Meijerink, A.; Langer, R.; Farokhzad, O. C.; Fayad, Z. A.; Mulder, W. J. Engineering of Lipid-Coated PLGA Nanoparticles with a Tunable Payload of Diagnostically Active Nanocrystals for Medical Imaging. *Chem. Commun. (Cambridge, U.K.)* **2012**, *48*, 5835–5837.